

Planck Galactic Cold Clumps at High Galactic Latitude

FENGWEI XU,¹ YUEFANG WU,¹ CHAO ZHANG,² XUNCHUAN LIU,^{1,3} TIE LIU,^{1,4,5} FANYI MENG,^{1,6} AND YU WANG¹

¹*Department of Astronomy, School of Physics, Peking University, Beijing, 100871, China*

²*Department of Astronomy, School of Physics and Astronomy, Yunnan University, Kunming, 650091, China*

³*Kavli Institute for Astronomy and Astrophysics, Peking University, Beijing 100871, China*

⁴*Korea Astronomy and Space Science Institute, 776 Daedeokdaero, Yuseong-gu, Daejeon 34055, Republic of Korea*

⁵*East Asian Observatory, 660 N.A'ohoku Place, Hilo, HI 96720, USA*

⁶*I. Physikalisches Institut, Universität zu Köln, Zùlpicher Str. 77, D-50937 Köln, Germany*

ABSTRACT

Forty-one Planck Galactic cold clumps (PGCCs) from the high Galactic latitude (HGal) were observed in ¹²CO, ¹³CO and C¹⁸O J=1-0 lines using the PMO 13.7-m telescope. All the targets were detected with all three lines, except for 25 without C¹⁸O. The location of PGCCs at high galactic latitude region (HGal) is not uniform but grouped. The distribution of all 41 clumps shows PGCCs extend our view to higher galactic region. The highest latitude we detected in this survey is $b = -71.43^\circ$. Fifty-one velocity components were obtained totally. Among all 41 detected HGLCs, four of them have asymmetric profiles and the highest asymmetric profile reaches to $b = -41.28^\circ$. Twenty-six clumps are mapped with both ¹²CO and ¹³CO while others were not because of the low ratio of signal to noise. Thirty-four cores were extracted from mapped HGLCs. The average excitation temperature T_{ex} is 11.6 K. The average line width of ¹³CO of HGLCs is 1.09 km s^{-1} and average line width of thermal velocity dispersion and non-thermal velocity dispersion are 0.18 km s^{-1} and 0.48 km s^{-1} respectively, showing that dynamical motion of these regions are dominated by turbulence. No cores are related to a young star (according to *SIMBAD*). Fourteen of HGal cores seems to be in a gravitationally bound state with virial criterion: $M_{LTE} > M_{vir}$. We classify two types of HGal cores with divisive relationship between α_{vir} and M_{LTE} . Type I cores tend to be in a quiet state while Type II cores are relatively diffuse. The distribution of two types of cores indicates that Type I cores are typical at HGal and Type II cores only show up in some filamentary structure.

Keywords: ISM: dark clouds - ISM: molecules - ISM: structure - stars: formation - ISM: high Galactic latitude

1. INTRODUCTION

Exploring the initial condition facilitates the study of star formation. Astronomers are encouraged to search for most primitive molecular clumps because they are close to initial evolution stage of forming stars and embed the prestellar cores. The prestellar cores and properties were widely involved since very early time (Myers & Benson 1983) and follow-up work concentrates on finding more primordial molecular cores. (Meng et al. 2013; Zhang et al. 2020; Könyves et al. 2015, 2020)

Molecular clouds at high Galactic latitude (hereafter HLCs) first observed by Blitz et al. (1984) just provide us with a set of translucent clouds (e.g. van Dishoeck & Black 1988) as a most early stage supplement of star formation. As

Blitz et al. indicates, the HCLs appear to be extraordinary young and may represent the earliest stages of molecular clouds condensing from the interstellar medium. There is no question that the molecular clouds in this region will lead us to an initial condition of star formation.

Apart from pursuing more primitive condition of molecular cores, another mission to study star formation of equal importance is to investigate the property and condition of the whole galaxy. Previous work have shown that the methanol masers which trace the massive star-forming region are rare at high latitude ($|b| > 2^\circ$, Yang et al.), which inspires that the latitude is a sensitive parameter for galactic star formation. However, in the past several decades, surveys of the molecular content of the Galaxy undertaken by many groups (Stark 1979; Burton & Gordon 1978; Blitz et al. 1982; Robinson et al. 1983; Israel et al. 1984; Sanders et al. 1984; Dame et al. 1987) have been of material either closely confined to the Galactic plane or limited to low galactic latitude (not

higher than 30° , Dame et al.), which reveals very little information about the molecular gas at HGal (Magnani et al. 1985). But the star formation still exists at HGal although relatively rare. Besides, the gas at HGal as a variable gas reservoir (Lilly et al. 2013) probably plays an important role in the cycle of the galactic gas. The property of the gas can be quite different from that in the galactic plane due to different roles in the cycle procedure. Hence, the knowledge of HLCs will definitely improve our understanding of the distribution of star formation regions or even gas cycle process in our galaxy.

Observing the high Galactic region begins with $^{12}\text{C}^{16}\text{O}$ ($J=1-0$) which is the strongest excited lines of all, together with other wavelength data available over the entire sky. Magnani et al. first believed the molecular clouds are optical dark and observed the CO line toward optical obscurations. After the pioneer works, many works followed (e.g. Keto & Myers 1986). Far-infrared data are also used as a probe for molecular clouds (Blitz et al. 1990; Reach et al. 1994). The following high-resolution observations toward these HLCs which managed to investigate the detailed information within 1pc demonstrated that the distribution of molecular clouds show smaller structures (Wouterloot et al. 2000). To explore the smaller size and study the star formation at high galactic latitude, CO observation of these HLCs with a high spatial resolution are needed. CO observations with the CfA 1.2 m telescope towards Polaris Flare revealing an extensive molecular clouds at high Galactic latitude are conducted by (Heithausen & Thaddeus 1990). The observation with CO and HI put forward that far-infrared ‘cirrus’ emission of Ursa comes from molecular and atomic cloud (de Vries et al. 1987). (Yamamoto et al. 2003) followed up with observation toward the HI filament region including MBM 53, 54, and 55 with approximately 141 square degree.

However, the research of HLCs demands far more investigation and information. On one hand, the overall and unbiased survey are always necessary; On the other hand, the grid spacing or sampling spacing are never enough to demand more accurate. But according to the previous work, it’s hard to achieve both, because more accuracy needs more time to integrate so that the all-sky especially mapping survey is technically unfeasible. Besides, there can be no signal detected in the considerable area, which produce a mass of time wasting. One doable method is to use the relatively accurate spacing telescope to detect the specified regions of HGal. And this is what we did as follows.

Planck surveys provide an unprecedentedly complete space distribution of sources. The all-sky nature of the Planck Galactic Cold Clumps (hereafter PGCCs) sample is particularly useful for studying the global properties of Galactic molecular gas or clouds. A follow-up study of 674 Early Cold Cores (hereafter ECC), part of Planck Early Re-

lease Compact Source catalog (Planck Collaboration et al. 2011a) was conducted using the 13.7-m telescope of the Purple Mountain Observatory (PMO) at Qinghai province. The $30''$ grid spacing satisfies the accuracy to detect the detailed structure of clumpy clouds. PGCCs also provide a plenty of early sources that are cold with dust temperature from 10 K to 15 K probably the coldest parts of ISM (Planck Collaboration et al. 2011b), which enables us to probe the characteristics of the prestellar phase or starless clumps (Wu et al. 2012). But the observation of Planck satellite only offers the continuum spectrum which ignore the velocity information of the sources. Fortunately, PMO observation provides all $^{12}\text{CO}(1-0)$, $^{13}\text{CO}(1-0)$, and $\text{C}^{18}\text{O}(1-0)$ lines in single point mode, and a part also in mapping mode. Besides, we also observe another two emission lines $\text{N}_2\text{H}^+(1-0)$ and $\text{C}_2\text{H}(1-0)$ for high galactic latitude as supplementary observation.

In this paper, we want to answer these question: how high latitude can star formation still exist or in what kind of process and phase of HLCs are? We report an investigation of 41 PGCCs at high galactic latitude. The samples are described in Section 2.1 and observational details in Section 2.2. The distribution of these 41 PGCCs will be given in Section 3.1. The line profiles and parameters are also discussed respectively in Section 3.2 and Section 3.3. The derived parameters and emission region parameters are calculated in Section 3.4 and Section 3.5. Further discussion follows in Section 4. Summary are in Section 5.

2. SAMPLES AND OBSERVATIONS

2.1. Samples

We selected the sample from the Early Cold Core Catalogue-Advanced Sample, in which PGCCs have large signal-to-noise ratio ($\text{SNR} > 15$). To make the observation with a sufficiently high elevation for the 13.7 m telescope at De Ling Ha, our samples were chosen from the ECC with a $\text{decl.} \geq -20^\circ$. There are 674 sources from the ECC that satisfy this criterion. The latitude of HGal is defined as $|b| > 25^\circ$ in regardless of longitude. In order to compare the characteristics and property of clumps at HGal with those at low galactic latitude, we extent the latitude b to lower latitude ($20^\circ < |b| < 25^\circ$) in the certain range of longitude ($|\Delta l| < 5^\circ$) furthermore.

2.2. Observations

Observations of 41 HGLCs were carried out, with the 13.7 m millimeter-wavelength telescope of Purple Mountain Observatory (PMO) in the $J=1-0$ transition of ^{12}CO , ^{13}CO and C^{18}O from April to May 2011 and December 2011 to January, 2012. The 3×3 -beam sideband separation Superconduction Spectroscopic Array Receiver system was used as the front end. The HPBW is 52 arcsec in the 115 GHz band. The mean beam efficiency is about 50%. The pointing accu-

racy is better than $5''$. The fast Fourier transform spectrometers (FFTSs) were used as the backend. Each FFTS with a total bandwidth of 1 GHz provides 16384 channels. The velocity resolutions are 0.16 km s^{-1} for ^{12}CO , and 0.17 km s^{-1} for ^{13}CO and C^{18}O . The ^{12}CO emission was observed in the upper sideband (USB) with the system temperature (T_{sys}) around 210 K, while the ^{13}CO and C^{18}O emissions were observed simultaneously in the lower sideband (LSB) with T_{sys} around 120 K. The typical rms was 0.2 K in T_A^* for ^{12}CO , and 0.1 K for ^{13}CO and C^{18}O . The on-the-fly (OTF) observing mode was applied. The antenna continuously scanned a region of $22' \times 22'$ centered on the PGCCs with a scanning rate of $20''$ per second. Because of the high rms noise level at the edges of OTF maps, only the central $14' \times 14'$ regions were used for analyses in this work. The data were reduced by CLASS and GREG in the GILDAS package. All statistical figures were plotted by open source Python package.

3. RESULTS

We made the observation towards 41 HGLCs of which the latitude is higher than 25° with 13.7 m telescope at De Ling Ha, Qinghai Province. Much higher than before latitude clumps were detected. The highest clump we detected is G126.65-71.43, of which the latitude reaches -71.43° , which means we found more extensive gas and now have a more overall view of the distribution of gas in the Galaxy. These 41 HGal PGCCs are not uniformly distributed along both galactic latitude and longitude. There are two complexes from the view of Latitude and also two from the view of Longitude in High Galactic Region $|b| > 25^\circ$.

The ^{12}CO (1-0) and ^{13}CO (1-0) emissions of all the clumps were detected, while C^{18}O emissions were detected only in the 16 HGLCs. The detection rate of C^{18}O in this region is 40%, much lower than 68% of 674 Planck cold clumps of the Early Cold Core Catalogue observed by Purple Mountain Observatory 13.7 m telescope, let alone 77.5% in Taurus, 81.5% in IQuad, 79.5% in ACent and 84.4% in IIQuad. The low detection probably indicates that the gas at high latitude is too diffuse and early developed to form a dense core inside.

Eight HGal PGCCs have double velocity components and one HGal PGCC has triple velocity components. In total, 51 velocity components were obtained in HGal. Centroid velocities of the clumps were obtained by Gaussian fitting. The kinematical distances were derived with the highest probabilities given by a Bayesian distance calculator¹ Galactic face-on position of the 41 clumps is shown in Figure. 1

The integrated intensity maps of CO are plotted and 12 of them are presented as sample maps in Figure , in which the clumps show different morphologies, such as isolated

cores, filamentary structures and also diffuse or full-coverage feature without certain boundary, which makes difficulty in defining a core. In this paper, we define a dense core, which have an isoline of 50% ^{13}CO peak intensity and are denser than the surrounding regions in the same clump. Velocity components of a PGCC are denoted as "a, b, c, ...", while the cores are labeled as "1, 2, 3, ...". Seventeen clumps contain only one dense core and nine contain more than one dense cores. In total, 34 cores were identified in twenty-six clumps.

3.1. Clumps Distribution

According to Dame et al.(1987), the distribution of the detected clumps are assigned to different molecular complexes. Six hundred seventy-four clumps observed with 13.7 m telescope at De Ling Ha were sort up into several complexes. With galactic latitude higher than 25° ($|b| > 25^\circ$), the clumps were classified as High Glat Region. There are 41 clumps from 674 sources that satisfy this criterion. The names and coordinates of 41 high latitude are listed in Table. One clump marked with "★" is without suitable background reference positions for the CO emission observations and are thus excluded in the further analysis. The highest clump we detected is G126.65-71.43 with $b = -71.43^\circ$. The average latitude of these clumps $\Sigma_{\text{clumps}}|b|$ lifts up to 37.77° . The total map covers the area of ????. The distribution of these 41 HGLCs is not uniform along the latitude as well as along the longitude. As Figure 1 shows, the detected clumps are seemingly assigned to two groups: one at positive latitude ($b > 0$) and one at negative latitude ($b < 0$). From Figure 2, the longitude of the detected clumps are mostly at the range of $90^\circ < l < 180^\circ$ and $0^\circ < l < 45^\circ$.

3.2. Line Profiles

All the HGLCs were observed with ^{12}CO , ^{13}CO and C^{18}O except for 25 without C^{18}O . With optically thin line (^{13}CO) and optically thick line (^{12}CO), we can define velocity component. Generally, a multi-peak optically thick molecular line can't be the compelling evidence of a multi-velocity detection. To confirm a multi-velocity source, a multi-peak optically thin lines are also needed. At the same time, the peaks of both ^{12}CO and ^{13}CO should be at about the same place. With this method, we define the velocity components of these 41 clumps. Most of the observed clumps have single velocity component in CO emission. Among the 41 clumps, 8 have double velocity components and only one have three velocity components and no clumps have more than three velocity components. The spectral line of each distinguishable components was fitted with a Gaussian function. Some molecular lines which depart from a Gaussian profile are analyzed further. For those lines with double peaks, we classified them as blue or red asymmetric profile if its higher peak skews to the blue or red side. Combining with an optically thin line, a

¹ <http://bessel.vlbi-astrometry.org/bayesian>

double-peaked optically thick line can be further identified as a blue profile if its higher peak is shifted blueward with $\delta V = (V_{thick} - V_{thin})/\Delta V_{thin} < -0.25$. A red profile would have $\delta V > 0.25$. Blue and red profiles are evidences for infall and outward motions. The spectral profile classifications are listed in last column of Table 2A and Table 3A.

3.3. Line Parameters

Gaussian fittings to the three CO lines for every velocity component at each clumps were made. Centroid velocity V_{lsr} , main beam brightness temperature T_b , and FWHM ΔV were obtained for all three CO lines, which are given in the Table 2A. Among 41 clumps, we only have map results of 26 clumps, because of the low signal to noise ratio of the rest. The ^{12}CO , ^{13}CO and C^{18}O spectra are extracted from the peak positions of the dense core we defined before. 4 Lines in $1' \times 1'$ of the peak region are study and shown on average. To investigate the parameters of defined cores, we also made Gaussian fittings to the three CO lines for every defined cores and the results are shown in the Table 3A. Centroid velocity of ^{13}CO was taken as the systematic velocity of each velocity component because $^{12}\text{CO}(1-0)$ line is optically thick and $\text{C}^{18}\text{O}(1-0)$ has low signal to noise ratio.

The statistical analyses of three CO lines are as follows and listed in Table???

3.4. Derived Parameters

The excitation temperatures (T_{ex}) and optical depths (τ) can be derived from the solution of the radiation transfer equation

$$T_b = \frac{h\nu}{k} \left[\frac{1}{\exp(h\nu/kT_{ex}) - 1} - \frac{1}{\exp(h\nu/kT_{bg}) - 1} \right] \times [1 - \exp(-\tau)]f, \quad (1)$$

where T_{bg} is the background temperature (2.73 K). Under assumptions that $^{12}\text{CO} J=1-0$ is optically thick ($\tau \gg 1$), beam filling factor f equals to 1, the excitation temperature can be expressed as

$$T_{ex} = \frac{h\nu}{k} \ln^{-1} \left\{ \left[\frac{kT_b(^{12}\text{CO})}{h\nu} + \frac{1}{\exp(h\nu/kT_{bg}) - 1} \right]^{-1} + 1 \right\}. \quad (2)$$

Under the condition of local thermodynamic equilibrium (LTE), ^{12}CO and ^{13}CO have the same excitation temperature. We can obtain optical depth of ^{13}CO ($\tau_{^{13}\text{CO}}$) by

$$\tau_{^{13}\text{CO}} = -\ln \left[1 - \frac{T_b(^{13}\text{CO})}{T_b(^{12}\text{CO})} \right]. \quad (3)$$

The T_{ex} of the 41 clumps range from 7 K to 22 K with a median value of ~ 11.7 K. The dust temperature (T_{dust}) of all PGCCs ranges from 5.8 to 20 K with a median value between 13 and 14.5 K. The similar temperature ranges between T_{ex} and T_{dust} indicate that the gas and dust are well coupled.

The column density of ^{13}CO ($N_{^{13}\text{CO}}$) and C^{18}O ($N_{\text{C}^{18}\text{O}}$) can be derived by

$$N = \frac{3k}{8\pi^3 B \mu_d^2} \frac{\exp(hBJ(J+1)/kT_{ex})}{J+1} \times \frac{T_{ex} + hB/3k}{1 - \exp(-h\nu/kT_{ex})} \int \tau_v dV, \quad (4)$$

where B , μ_d and J are the rotational constant, permanent dipole moment of the molecule and the rotational quantum number of the lower state in the observed transition. We made an assumption that the optical depth doesn't change a lot with velocity. With equation (1) applied with ^{13}CO , optical depth can be expressed as:

$$\tau = \frac{\tau}{1 - \exp(-\tau)} \frac{T_b(^{13}\text{CO})}{F(T_{ex})} \quad (5)$$

where $F(T_{ex})$ is the abbreviation of

$$F(T_{ex}) = \frac{h\nu_{13}}{k} \left[\frac{1}{\exp(h\nu_{13}/kT_{ex}) - 1} - \frac{1}{\exp(h\nu_{13}/kT_{bg}) - 1} \right] \quad (6)$$

Adopting the typical abundance ratios, $[\text{H}_2]/[^{13}\text{CO}] = 89 \times 10^4$ for the solar neighborhood, the column density of hydrogen (N_{H_2}) can be calculated. We use ^{13}CO to calculate H_2 column densities, as listed in Table.

The one-dimensional velocity dispersion of ^{13}CO is given by

$$\sigma_{^{13}\text{CO}} = \frac{\Delta V_{^{13}\text{CO}}}{\sqrt{8 \ln 2}}. \quad (7)$$

The thermal (σ_{Th}) and non-thermal (σ_{NT}) velocity dispersions can be calculated by

$$\sigma_{Th} = \sqrt{\frac{kT_{ex}}{m_H \mu}}, \quad (8)$$

$$\sigma_{NT} = \left[\sigma_{^{13}\text{CO}}^2 - \frac{kT_{ex}}{m_{^{13}\text{CO}}} \right]^{1/2}, \quad (9)$$

where m_H is the mass of atomic hydrogen, μ is the mean weight of molecule which equals to 2.33

$$\sigma_{3D} = \sqrt{3(\sigma_{Th}^2 + \sigma_{NT}^2)}. \quad (10)$$

All the above derived parameters are listed in Table 4A

3.5. Emission region parameters

The ^{12}CO , ^{13}CO and C^{18}O spectra are extracted from the peak positions of the dense core we defined before in total 26 mapped clumps. 4 Lines in $1' \times 1'$ of the peak region are study and shown on average. Figure??? presents sample spectra of ??? cores. As the single point observation analyses did, we

also derive the peak line parameters with Gaussian fitting in Table 5A. The offset peak positions relative to the PGCCs are estimated from isoline with 50% to 90% of the peak integrated intensity. The area S of the cores were defined by 50% isoline with by drawing polygons in *CLASS*. The core radius can be calculated as $R = \sqrt{\frac{S}{\pi}}$, and volume density can be derived through $n_{\text{H}_2} = N_{\text{H}_2}/2R$, under the assumption of homogeneous spherical material distribution.

The gas mass can be obtained directly from

$$M = \frac{4}{3}\pi R^3 m_{\text{H}} \mu n_{\text{H}_2}. \quad (11)$$

Assuming that the cores are gravitationally bound isothermal spheres with uniform density and supported solely by random motions, we can calculate the virial mass M_{vir} as

$$M_{\text{vir}} = \frac{5R}{3\gamma G} \sigma_{3D}^2, \quad (12)$$

where G is the gravitational constant. Assuming the density profile follows $\rho \propto R^{-2}$, γ equals to 5/3.

In molecular clouds, thermal pressure, turbulence and magnetic field can support the gas against gravity collapse. Taking thermal pressure and turbulence into account, the Jeans mass can be expressed as following

$$\frac{M_{\text{Jeans}}}{M_{\odot}} \approx 1.0 a_J \left(\frac{T_{\text{eff}}}{10K} \right)^{3/2} \left(\frac{\mu}{2.33} \right)^{-1/2} \left(\frac{n}{10^4 \text{cm}^{-3}} \right)^{-1/2}, \quad (13)$$

where a_J is a dimensionless parameter of the order unity, n is the volumn density of H_2 , and the effective kinematic temperature T_{eff} is adopted as $\frac{C_{s,\text{eff}}^2 \mu m_{\text{H}}}{k}$. The effective sound speed $C_{s,\text{eff}}$ is adopted as $[(\sigma_{\text{NT}})^2 + (\sigma_{\text{Th}})^2]^{1/2}$ to account for support of turbulence.

The radius, volumn density, gas mass, virial mass and Jeans mass are listed in Table??? and their statistics are listed in Table???

4. DISCUSSION

4.1. Galactic distribution

The whole map of HGLCs is shown in Figure???. Compare to prior CO survey (Heithausen et al. 1993 & Yamamoto et al. 2003), we found much higher clumps. The highest clump we detected is G126.65-71.43 with $b = -71.43^\circ$. The average latitude of these clumps $\frac{\sum \text{clumps} |b|}{N_{\text{clumps}}}$ lifts up to 36.87° . The total map covers the area of ???. Our survey extends our view to a larger range of the galaxy, not limited to the disk with low latitude. As for line profile, the highest asymmetric profile reaches to $b = -41.28^\circ$. Asymmetric profile sometimes indicates the probable star formation activities. With respect to dense cores, the highest gravitationally binding core reaches to the latitude of $b = +37.02^\circ$. Gravitationally stability might increase the star formation probability of

a core. Both the asymmetric line profile and the gravitational stability inform that the star formation activities can still happen at high galactic latitude. Because the high galactic region is lack of survey data of, we can only show the Planck cold clumps in the HGal map like Figure 1 and Figure 2.

4.2. Emission lines

All the HGLCs were observed with ^{12}CO , ^{13}CO and C^{18}O except for 25 without C^{18}O . The detection rate of CO is much higher than before, compared to CO survey where only 13% of the CO survey sample have been detected in the second quadrant (Heithausen et al. 1993). High detection rate indicates that Plank Cold Galactic CLumps (PGCCs) are a group of good tracers to CO gas emission region. However, the detection rate of C^{18}O (50%) decreases much to only 40%, compared to 68% of the total sample-674 PGCCs, let alone 77.5% in Taurus, 81.5% in IQuad, 79.5% in ACent and 84.4% in IIQuad. Because C^{18}O generally appears in the dense gas cores with relatively high density, the low detection of C^{18}O should infer that the gas at high galactic latitude is relatively diffuse compared to that on the galactic plane.

As for line profile, we use the optically thin line ^{13}CO and optically thick line ^{12}CO to define different types of line profile. We concentrate much on the blue or red profile which may refer to the potential star formation activities: inflow and outflow respectively. (Here we can supply some mechanism with figure)

4.3. Non-thermal motion

Analyzing non-thermal motions of dense cores is useful for the understanding of many physical processes including star formation and heating transport. Systematical motions originated from star forming activities such as infall motions and outflows can broaden the non-thermal velocity dispersion. However, these PGCCs are not very active when compared with typical star forming regions. The non-thermal motions in these clumps are therefore mainly contributed by turbulent motion.

The ratio of non-thermal to thermal velocity dispersion $R_p = \sigma_{\text{NT}}^2 / \sigma_{\text{Th}}^2$ can be used to estimate the ratio of pressure contributed from the non-thermal and thermal motions. Our results show that R_p are larger than 1 for all the sources with average value of 8, and thus turbulences in PGCCs in both regions are typically supersonic. The increasing trends of σ_{NT} and R_p with respect to N_{H_2} are still waited to be discovered. It implies that the non-thermal pressure is more dominant in denser cores.

Since Larson (1981MNRAS.194..809L) put forward the idea that the internal velocity dispersion is correlated with its region size from 0.1 to 100 pc in a power-law form, lots of works were followed. We can also test this result at HGal region.

4.4. *core status*

5. SUMMARY

We have performed a single point survey in J=1-0 transition of ^{12}CO , ^{13}CO and C^{18}O with PMO 13.7-m telescope toward 41 Planck Galactic cold clumps (PGCCs) at high galactic latitude. Of 41 HGLCs, 26 of them also have mapping observations. All the sources are located at high galactic latitude $|b| > 25^\circ$. ^{12}CO and ^{13}CO lines were detected in all of them, while C^{18}O line was detected in 16 of HGLCs with the detection rate about 40%. Fifty-one velocity components are identified in total. We identified 34 dense cores from the velocity integrated intensity maps. The parameters of detected lines and identified cores were derived. We have discussed their properties, morphologies. The main findings are summarized as follows.

1. Our samples are all located at the high galactic latitude region with $|b| > 25^\circ$. We detected the highest clump G126.65-71.43 with $b = -71.43^\circ$ by single point observation, and the highest clump G089.03-41.28 with $b = -41.28^\circ$ by mapping observation.

2. The excitation temperature (T_{ex}) of High Galactic Latitude Cores ranges from 7.6 to 22.4 K respectively. The excitation temperature are similar to the dust temperature (T_{dust}). However, the median value of the T_{ex} are smaller than that of T_{dust} , suggesting that gas and dust are well coupled in these cores and gas might be heated by dust.
3. The non-Gaussian profiles, including 2 blue profiles and 2 red profiles are detected at high galactic latitude. We have identified ??? cores with associated objects.
4. Non-thermal velocity dispersion and the non-thermal to thermal pressure increases with H_2 column density indicates that the non-thermal pressure is more dominant in denser cores. PGCC cores in both regions are turbulence dominated.
5. Core mass function fittings are not currently studied. More results are still waited to be concluded.

We are grateful to the staff at the Qinghai Station of PMO for their assistance during the observations. We also thank Yuefang Wu for the suggestion and idea about this study. We thank Chao Zhang, Xunchuan Liu and Yu Wang for software support such as CLASS and GREG in the GILDAS and Python.

REFERENCES

- Blitz, L., Bazell, D., & Desert, F. X. 1990, *ApJL*, 352, L13, doi: [10.1086/185682](https://doi.org/10.1086/185682)
- Blitz, L., Fich, M., & Stark, A. A. 1982, *ApJS*, 49, 183, doi: [10.1086/190795](https://doi.org/10.1086/190795)
- Blitz, L., Magnani, L., & Mundy, L. 1984, *ApJL*, 282, L9, doi: [10.1086/184293](https://doi.org/10.1086/184293)
- Burton, W. B., & Gordon, M. A. 1978, *A&A*, 63, 7
- Dame, T. M., Ungerechts, H., Cohen, R. S., et al. 1987, *ApJ*, 322, 706, doi: [10.1086/165766](https://doi.org/10.1086/165766)
- de Vries, H. W., Heithausen, A., & Thaddeus, P. 1987, *ApJ*, 319, 723, doi: [10.1086/165492](https://doi.org/10.1086/165492)
- Heithausen, A., & Thaddeus, P. 1990, *ApJL*, 353, L49, doi: [10.1086/185705](https://doi.org/10.1086/185705)
- Israel, F. P., de Graauw, T., van der Biezen, J., et al. 1984, *A&A*, 134, 396
- Keto, E. R., & Myers, P. C. 1986, *ApJ*, 304, 466, doi: [10.1086/164181](https://doi.org/10.1086/164181)
- Könyves, V., André, P., Men'shchikov, A., et al. 2015, *A&A*, 584, A91, doi: [10.1051/0004-6361/201525861](https://doi.org/10.1051/0004-6361/201525861)
- Könyves, V., André, P., Arzoumanian, D., et al. 2020, *A&A*, 635, A34, doi: [10.1051/0004-6361/201834753](https://doi.org/10.1051/0004-6361/201834753)
- Lilly, S. J., Carollo, C. M., Pipino, A., Renzini, A., & Peng, Y. 2013, *ApJ*, 772, 119, doi: [10.1088/0004-637X/772/2/119](https://doi.org/10.1088/0004-637X/772/2/119)
- Magnani, L., Blitz, L., & Mundy, L. 1985, *ApJ*, 295, 402, doi: [10.1086/163385](https://doi.org/10.1086/163385)
- Meng, F., Wu, Y., & Liu, T. 2013, *The Astrophysical Journal Supplement Series*, 209, 37, doi: [10.1088/0067-0049/209/2/37](https://doi.org/10.1088/0067-0049/209/2/37)
- Myers, P. C., & Benson, P. J. 1983, *ApJ*, 266, 309, doi: [10.1086/160780](https://doi.org/10.1086/160780)
- Planck Collaboration, Ade, P. A. R., Aghanim, N., et al. 2011a, *A&A*, 536, A23, doi: [10.1051/0004-6361/201116472](https://doi.org/10.1051/0004-6361/201116472)
- , 2011b, *A&A*, 536, A22, doi: [10.1051/0004-6361/201116481](https://doi.org/10.1051/0004-6361/201116481)
- Reach, W. T., Koo, B.-C., & Heiles, C. 1994, *ApJ*, 429, 672, doi: [10.1086/174353](https://doi.org/10.1086/174353)
- Robinson, B. J., Manchester, R. N., Whiteoak, J. B., & McCutcheon, W. H. 1983, *Astrophysics and Space Science Library*, Vol. 105, CO distribution along the southern galactic plane, ed. W. B. Burton & F. P. Israel, 1–15, doi: [10.1007/978-94-009-7217-9_1](https://doi.org/10.1007/978-94-009-7217-9_1)
- Sanders, D. B., Solomon, P. M., & Scoville, N. Z. 1984, *ApJ*, 276, 182, doi: [10.1086/161602](https://doi.org/10.1086/161602)
- Stark, A. A. 1979, PhD thesis, Princeton Univ., NJ.
- van Dishoeck, E. F., & Black, J. H. 1988, *ApJ*, 334, 771, doi: [10.1086/166877](https://doi.org/10.1086/166877)

- Wouterloot, J. G. A., Heithausen, A., Schreiber, W., & Winnewisser, G. 2000, A&AS, 144, 123, doi: [10.1051/aas:2000200](https://doi.org/10.1051/aas:2000200)
- Wu, Y., Liu, T., Meng, F., et al. 2012, ApJ, 756, 76, doi: [10.1088/0004-637X/756/1/76](https://doi.org/10.1088/0004-637X/756/1/76)
- Yamamoto, H., Onishi, T., Mizuno, A., & Fukui, Y. 2003, ApJ, 592, 217, doi: [10.1086/375128](https://doi.org/10.1086/375128)
- Yang, K., Chen, X., Shen, Z.-Q., et al. 2017, ApJ, 846, 160, doi: [10.3847/1538-4357/aa8668](https://doi.org/10.3847/1538-4357/aa8668)
- Zhang, C., Wu, Y., Liu, X., et al. 2020, ApJS, 247, 29, doi: [10.3847/1538-4365/ab720b](https://doi.org/10.3847/1538-4365/ab720b)

Table 1. Survey High galactic ECC clump Catalogue

Name	Glon	Glat	R.A.(J2000)	Decl.(J2000)	R.A.(B1950)	Decl.(B1950)	CO
	deg	deg	h:m:s	d:m:s	h:m:s	d:m:s	
(1)	(2)	(3)	(4)	(5)	(6)	(7)	(8)
G118.25-52.70	118.25124	-52.705425	00 39 55.42	+10 03 41.94	00 37 19.73	+09 47 13.89	Single
G126.65-71.43	126.65636	-71.439209	00 56 13.82	-08 36 07.67	00 53 42.53	-08 52 21.24	Single
G127.31-70.09	127.31833	-70.095444	00 57 27.24	-07 16 29.84	00 54 55.63	-07 32 42.13	Single
G131.35-45.73	131.35713	-45.734646	01 15 57.51	+16 44 08.07	01 13 17.42	+16 28 18.47	Single
G133.72-45.31	133.72574	-45.315117	01 23 04.84	+16 53 32.68	01 20 24.08	+16 37 53.49	Single
G145.08-39.30	145.08543	-39.306114	02 04 00.04	+20 25 25.62	02 01 13.71	+20 11 03.42	Single&Mapping
G150.35-38.06	150.35887	-38.063641	02 22 11.93	+19 55 36.57	02 19 24.33	+19 41 57.58	Single
G151.58-38.58	151.58934	-38.586674	02 24 53.06	+19 01 47.06	02 22 05.92	+18 48 14.91	Single&Mapping
G153.74+35.91	153.74266	35.915295	08 36 34.59	+62 26 27.09	08 32 20.45	+62 36 52.58	Single&Mapping
G156.42+32.53	156.42332	32.531315	08 06 27.98	+60 34 20.05	08 02 12.51	+60 42 57.52	Single&Mapping
G158.77-33.30	158.7744	-33.308964	02 57 33.29	+20 38 31.01	02 54 42.16	+20 26 30.43	Single
G158.88-34.18	158.88426	-34.183754	02 55 48.23	+19 51 50.97	02 52 57.95	+19 39 45.12	Single&Mapping
G158.97-33.01	158.97215	-33.019318	02 58 50.03	+20 47 23.13	02 55 58.66	+20 35 26.45	Single&Mapping
G159.23-34.49	159.23582	-34.499992	02 56 04.75	+19 26 23.35	02 53 14.84	+19 14 18.34	Single&Mapping
G159.41-34.36	159.41161	-34.364319	02 56 54.67	+19 28 15.70	02 54 04.66	+19 16 13.20	Single&Mapping
G159.58-32.84	159.58739	-32.841549	03 01 05.17	+20 38 43.23	02 58 13.76	+20 26 53.47	Single&Mapping
G159.67-34.31	159.67528	-34.319141	02 57 46.94	+19 23 09.02	02 54 56.94	+19 11 09.16	Single&Mapping
G160.64-35.04	160.64207	-35.044933	02 58 48.02	+18 20 11.95	02 55 58.90	+18 08 15.22	Single&Mapping
G161.43-35.59	161.43309	-35.593529	02 59 41.08	+17 30 58.04	02 56 52.65	+17 19 04.04	Single&Mapping
G161.85-35.75	161.85057	-35.754246	03 00 26.79	+17 11 16.08	02 57 38.60	+16 59 24.43	Single&Mapping
G162.64-31.67	162.64159	-31.672619	03 12 56.11	+20 04 33.85	03 10 04.36	+19 53 21.59	Single&Mapping
G165.91-44.02	165.91882	-44.027889	02 50 21.82	+08 41 43.64	02 47 41.31	+08 29 21.83	Single
G173.32+31.27	173.3203	31.278992	08 03 20.34	+46 11 45.20	07 59 46.38	+46 20 12.22	Single
G173.91+31.16	173.91356	31.169939	08 03 07.66	+45 40 41.82	07 59 34.74	+45 49 08.07	Single
G182.54-25.34	182.54881	-25.344492	04 23 04.85	+12 13 03.09	04 20 18.04	+12 06 06.23	Single
G203.57-30.08	203.57664	-30.086176	04 47 58.28	-05 56 06.84	04 45 31.19	-06 01 21.77	Single
G210.67-36.77	210.67381	-36.772038	04 34 00.52	-14 10 28.57	04 31 42.53	-14 16 40.54	Single
G210.89-36.53	210.89354	-36.539547	04 35 10.69	-14 14 37.73	04 32 52.81	-14 20 44.94	Single

*No suitable background reference positions for the CO emission observations and are thus excluded in the analysis

NOTE—Only a part of clumps are shown in this table.

Table 2A. Single Point Line parameters of HGLCs

Source	$T_b(^{12}\text{CO})$	$V_{lsr}(^{12}\text{CO})$	$\Delta V_{12\text{CO}}$	$T_b(^{13}\text{CO})$	$V_{lsr}(^{13}\text{CO})$	$\Delta V_{13\text{CO}}$	$T_b(\text{C}^{18}\text{O})$	$V_{lsr}(\text{C}^{18}\text{O})$	$\Delta V_{\text{C}^{18}\text{O}}$	profile ^a
	K	(km s ⁻¹)	(km s ⁻¹)	K	(km s ⁻¹)	(km s ⁻¹)	K	(km s ⁻¹)	(km s ⁻¹)	
(1)	(2)	(3)	(4)	(5)	(6)	(7)	(8)	(9)	(10)	(11)
G089.03-41.28	-4.88(0.02)	2.87(0.04)	3.3(0.13)	-4.63(0.03)	1.93(0.06)	1.09(0.08)	BP
G126.65-71.43	-11.97(0.02)	0.78(0.04)	3.27(0.2)	-11.99(0.03)	0.63(0.06)	1.05(0.12)
G127.31-70.09	-8.03(0.02)	1.97(0.05)	2.6(0.15)	-8.09(0.05)	1.31(0.13)	0.59(0.09)
G131.35-45.73	-8.02(0.02)	2.54(0.04)	3.36(0.15)	-8.19(0.03)	1.82(0.07)	1.00(0.08)
G133.72-45.31	-8.62(0.02)	1.51(0.04)	3.62(0.18)	-8.47(0.01)	0.62(0.03)	1.66(0.09)	-8.44(0.06)	0.38(0.11)	0.28(0.09)	...
G145.08-39.30a	6.03(0.02)	0.53(0.04)	1.65(0.16)	6.21(0.01)	0.43(0.03)	1.19(0.09)	Dob
G145.08-39.30b	7.49(0.02)	0.9(0.05)	2.3(0.16)	7.11(0.01)	0.58(0.02)	2.1(0.09)	Dob
G150.35-38.06	5.16(0.01)	1.66(0.03)	3.89(0.14)	5.16(0.01)	0.96(0.02)	2.56(0.09)	5.1(0.05)	0.42(0.1)	0.33(0.09)	...
G151.58-38.58a	4.2(0.01)	0.58(0.03)	2.18(0.13)	Dob
G151.58-38.58b	5.63(0.01)	1.25(0.03)	3.51(0.13)	5.53(0.01)	0.67(0.04)	1.57(0.09)	Dob
G153.74+35.91	-2.09(0.02)	1.23(0.05)	3.4(0.24)	-2.13(0.03)	0.72(0.06)	1.25(0.14)	-2.58(0.08)	0.36(0.2)	0.27(0.13)	...
G156.42+32.53	-0.3(0.03)	2.09(0.06)	1.94(0.13)	-0.21(0.04)	1.32(0.1)	0.67(0.08)
G158.77-33.30a	-2.55(0.03)	2.69(0.07)	2.88(0.17)	-2.48(0.02)	1.47(0.04)	2.31(0.1)	-2.41(0.05)	0.72(0.11)	0.49(0.1)	Dob
G158.77-33.30b	1.22(0.03)	1.73(0.08)	2.39(0.17)	1.32(0.09)	1.00(0.25)	0.31(0.1)	Dob
G158.88-34.18	-4.61(0.03)	2.5(0.06)	3.41(0.19)	-5.13(0.02)	1.02(0.05)	1.92(0.13)	-5.29(0.06)	0.44(0.13)	0.4(0.12)	...
G158.97-33.01a	-2.59(0.01)	1.14(0.02)	2.70(0.10)	-2.88(0.03)	0.58(0.06)	1.33(0.08)	T
G158.97-33.01b	0.37(0.02)	1.01(0.05)	1.51(0.10)	T
G158.97-33.01c	1.94(0.00)	1.39(0.05)	1.70(0.10)	T
G159.23-34.49a	-5.06(0.04)	3.46(0.1)	3.44(0.16)	-5.09(0.01)	1.6(0.03)	3.08(0.1)	-5.09(0.03)	0.99(0.08)	0.72(0.09)	Dob
G159.23-34.49b	-2.31(0.03)	1.69(0.06)	2.68(0.16)	-2.71(0.03)	1.11(0.06)	1.08(0.1)	Dob
G159.41-34.36a	-5.34(0.02)	1.65(0.04)	4.13(0.18)	-5.21(0.01)	0.95(0.02)	3.04(0.09)	-5.22(0.02)	0.51(0.05)	0.92(0.09)	Dob
G159.41-34.36b	0.22(0.03)	1.11(0.06)	2.02(0.18)	0.33(0.02)	0.25(0.07)	0.6(0.09)	Dob
G159.58-32.84	3.79(0.02)	2.42(0.04)	3.5(0.14)	4.02(0.03)	1.38(0.07)	1.15(0.09)	RA
G159.67-34.31	-0.95(0.02)	2.07(0.04)	3.44(0.16)	-1.42(0.01)	0.93(0.03)	2.29(0.1)	-1.38(0.06)	0.38(0.1)	0.32(0.1)	...
G160.64-35.04	-4.49(0.02)	0.99(0.04)	2.78(0.16)	-4.45(0.01)	0.55(0.03)	1.57(0.08)
G161.43-35.59	-5.82(0.01)	0.88(0.02)	4.38(0.14)	-5.83(0.01)	0.58(0.01)	2.89(0.09)
G161.85-35.75	-6.47(0.01)	0.79(0.03)	3.47(0.15)	-6.59(0.01)	0.53(0.01)	2.93(0.09)	-6.65(0.03)	0.32(0.09)	0.41(0.09)	...
G162.64-31.67	-0.88(0.01)	0.94(0.02)	3.73(0.16)	-0.9(0.03)	0.67(0.06)	0.8(0.09)
G165.91-44.02	-6.07(0.02)	2.53(0.04)	3.17(0.14)	-5.85(0.02)	1.38(0.06)	1.41(0.09)
G173.32+31.27a	-8.72(0.01)	0.51(0.03)	1.79(0.13)	-8.75(0.03)	0.33(0.07)	0.42(0.08)	Dob
G173.32+31.27b	-1.77(0.07)	1.15(0.18)	0.58(0.13)
G173.91+31.16	-8.38(0.01)	0.72(0.03)	3.63(0.18)	-8.33(0.01)	0.56(0.03)	1.6(0.09)
G182.54-25.34	1.38(0.02)	2.07(0.05)	2.99(0.17)	1.06(0.05)	1.45(0.1)	0.64(0.09)	RP
G203.57-30.08	-5.02(0.01)	1.04(0.01)	6.29(0.15)	-4.94(0.01)	0.72(0.01)	3.98(0.09)	-4.95(0.02)	0.51(0.04)	1.27(0.09)	...
G210.67-36.77	0.6(0.02)	0.96(0.04)	5.36(0.34)	0.47(0.01)	0.6(0.02)	2.99(0.15)	0.45(0.06)	0.24(0.09)	0.45(0.17)	RP
G210.89-36.53	0.37(0.01)	0.99(0.02)	5.38(0.19)	0.33(0.01)	0.84(0.02)	3.8(0.1)	0.15(0.02)	0.4(0.05)	1.1(0.11)	...

^a The abbreviations are: RP: red profile; Dob: double velocity components. RA: red asymmetry

Note—Only a part of clumps are shown in this table.

Table 3A. Line parameters of core centers

source	xoffset	yoffset	distance	size	$T_b(^{12}\text{CO})$	$V_{lsr}(^{12}\text{CO})$	$\Delta V_{12\text{CO}}$	$T_b(^{13}\text{CO})$	$V_{lsr}(^{13}\text{CO})$	$\Delta V_{13\text{CO}}$	profile ^a
	(arcmin)	(arcmin)	(pc)	(pc)	(K)	(km s ⁻¹)	(km s ⁻¹)	(K)	(km s ⁻¹)	(km s ⁻¹)	
(1)	(2)	(3)	(4)	(5)	(6)	(7)	(8)	(9)	(10)	(11)	(12)
G004.15+35.77.1	149.8	-176.4	1700.0	1.136	18.93	2.46	1.66	5.74	2.59	1.56	...
G004.17+36.67.1	35.9	0.8	1640.0	1.239	9.96	2.45	0.98	6.02	2.36	0.68	...
G004.54+36.74.1	23.2	61.6	1560.0	1.262	8.61	2.38	1.16	5.10	2.47	0.82	...
G004.81+37.02.1	235.9	-57.4	2150.0	1.895	10.27	3.17	2.08	5.86	3.27	1.22	BP
G006.04+36.74.1	121.9	-244.7	1190.0	0.634	10.66	2.26	2.05	6.28	2.50	1.12	...
G008.43+36.35.1	63.7	-67.5	300.0	0.332	8.59	1.01	0.80	5.62	0.97	0.51	...
G011.40+36.19.1	-88.2	38.8	620.0	0.451	8.16	2.39	1.16	4.16	2.41	0.87	...
G089.03-41.28.1	-80.6	-62.4	3660.0	0.376	11.21	-4.89	2.44	2.75	-5.05	2.71	BP
G101.62-28.84.1	72.2	317.7	1700.0	0.635	8.67	-5.76	1.36	2.73	-5.87	0.91	...
G101.62-28.84.2	-20.6	80.9	1700.0	0.727	8.58	-5.86	1.18	3.09	-5.87	0.80	...
G101.62-28.84.3	-23.0	-116.8	1700.0	0.784	7.39	-5.88	1.27	2.48	-5.87	0.88	...
G102.72-25.98.1	125.0	-29.0	1580.0	1.405	8.18	-7.27	2.24	2.44	-7.27	1.89	...
G145.08-39.30.1	-93.2	-29.5	650.0	0.434	11.64	6.73	1.43	5.37	6.93	1.14	...
G151.58-38.58.1	-52.7	213.5	640.0	0.203	8.42	5.41	1.37	3.23	5.46	0.78	...
G151.58-38.58.2	-57.8	-9.3	640.0	0.388	8.59	5.66	1.33	2.97	5.53	1.03	RP
G151.58-38.58.3	233.3	-300.4	640.0	0.246	6.85	4.77	1.59	1.62	4.77	1.66	...
G151.58-38.58.4	-351.5	5.9	640.0	0.164	7.89	4.83	1.51	1.36	5.01	1.90	...
G153.74+35.91.1	-15.4	151.6	600.0	0.293	8.05	-2.14	1.25	2.77	-2.16	0.79	...
G156.42+32.53.1	231.8	-107.6	200.0	0.108	5.25	-0.81	1.23	1.73	-0.79	0.82	...
G158.77-33.30.1	-127.1	-111.1	600.0	0.536	6.88	-2.93	3.07	4.41	-2.79	2.29	...
G158.88-34.18.1	-94.5	122.3	1180.0	0.756	8.39	-5.26	1.62	5.82	-5.33	0.97	...
G158.88-34.18.2	133.3	-90.1	1180.0	0.996	9.59	-5.75	2.25	4.72	-5.52	1.61	...
G158.97-33.01.1	-128.7	0.8	690.0	0.171	6.76	1.56	1.67	2.29	1.57	0.75	...
G159.23-34.49a.1	86.5	43.9	1170.0	1.456	8.22	-5.08	3.05	6.11	-5.23	1.88	...
G159.23-34.49b.1	0.4	61.6	680.0	0.542	5.18	-2.50	1.68	2.27	-2.70	1.60	...
G159.41-34.36.1	-103.4	-146.0	1200.0	1.024	9.67	-5.04	1.68	6.28	-5.02	1.18	...
G159.58-32.84.1	-15.8	94.6	500.0	0.246	4.34	3.44	2.03	1.12	3.74	1.39	RA
G159.67-34.31.1	24.7	40.9	430.0	0.334	9.90	-1.17	1.70	4.10	-1.22	1.33	RA
G160.64-35.04.1	-65.4	271.7	1100.0	0.411	6.56	-5.07	0.83	3.63	-5.08	0.71	...
G160.64-35.04.2	-78.1	-115.6	1100.0	0.656	6.90	-4.69	1.38	2.67	-4.63	0.96	...
G160.64-35.04.3	-288.2	31.2	1100.0	0.503	5.84	-4.91	1.31	2.44	-4.92	0.96	...
G161.43-35.59.1	66.2	185.6	1490.0	0.755	7.01	-5.88	1.17	3.63	-5.86	0.95	...
G161.43-35.59.2	35.9	-21.9	1490.0	1.033	10.45	-5.90	0.76	6.99	-5.86	0.59	...
G161.85-35.75.1	-62.9	13.5	1740.0	0.814	6.67	-6.29	1.59	4.40	-6.58	0.86	...
G162.64-31.67.1	-62.9	-57.4	340.0	0.114	5.94	-0.92	1.14	2.21	-0.90	0.59	...
G182.54-25.34.1	24.1	58.0	1500.0	0.469	9.85	0.78	1.96	2.34	0.52	1.54	RP

^a The abbreviations are: RP: red profile; BP: blue profile; RA: red asymmetry

NOTE—All the cores are shown in the table.

Table 4A. Derived parameters at the core center

source	T_{ex}	τ_{13}	N_{H_2}	σ_{NT}	σ_{Th}	$\sigma_{3\text{D}}$
	(K)		(10^{21} cm^{-2})	(km s^{-1})	(km s^{-1})	(km s^{-1})
(1)	(2)	(3)	(4)	(5)	(6)	(7)
G004.15+35.77_1	22.42	0.361	14.12	0.66	0.26	1.23
G004.17+36.67_1	13.38	0.927	6.01	0.28	0.20	0.60
G004.54+36.74_1	12.00	0.897	5.74	0.34	0.19	0.68
G004.81+37.02_1	13.69	0.845	10.26	0.51	0.20	0.96
G006.04+36.74_1	14.09	0.889	10.44	0.47	0.21	0.89
G008.43+36.35_1	11.98	1.062	4.21	0.21	0.19	0.49
G011.40+36.19_1	11.55	0.713	4.51	0.36	0.19	0.71
G089.03-41.28_1	14.64	0.281	8.59	1.15	0.21	2.02
G101.62-28.84_1	12.07	0.378	2.71	0.38	0.19	0.74
G101.62-28.84_2	11.97	0.447	2.78	0.33	0.19	0.67
G101.62-28.84_3	10.76	0.409	2.30	0.37	0.18	0.71
G102.72-25.98_1	11.57	0.354	4.88	0.80	0.19	1.42
G145.08-39.30_1	15.08	0.619	8.39	0.48	0.21	0.91
G151.58-38.58_1	11.81	0.484	2.86	0.33	0.19	0.65
G151.58-38.58_2	11.98	0.424	3.40	0.43	0.19	0.82
G151.58-38.58_3	10.21	0.270	2.60	0.70	0.18	1.26
G151.58-38.58_4	11.27	0.189	2.50	0.80	0.19	1.43
G153.74+35.91_1	11.43	0.422	2.38	0.33	0.19	0.66
G156.42+32.53_1	8.56	0.400	1.38	0.34	0.16	0.66
G158.77-33.30_1	10.24	1.024	13.68	0.97	0.18	1.71
G158.88-34.18_1	11.78	1.183	8.65	0.41	0.19	0.78
G158.88-34.18_2	13.00	0.678	9.86	0.68	0.20	1.23
G158.97-33.01_1	10.12	0.414	1.77	0.31	0.18	0.62
G159.23-34.49a_1	11.61	1.360	18.76	0.80	0.19	1.42
G159.23-34.49b_1	8.49	0.577	3.82	0.68	0.16	1.21
G159.41-34.36_1	13.08	1.048	11.31	0.50	0.20	0.93
G159.58-32.84_1	7.61	0.298	1.41	0.59	0.15	1.05
G159.67-34.31_1	13.31	0.535	6.72	0.56	0.20	1.03
G160.64-35.04_1	9.91	0.806	3.14	0.30	0.17	0.60
G160.64-35.04_2	10.26	0.489	2.75	0.40	0.18	0.76
G160.64-35.04_3	9.17	0.541	2.48	0.40	0.17	0.76
G161.43-35.59_1	10.37	0.729	4.14	0.40	0.18	0.76
G161.43-35.59_2	13.87	1.105	6.65	0.24	0.21	0.55
G161.85-35.75_1	10.02	1.078	5.20	0.36	0.18	0.70

NOTE—All of the cores are shown in the table.

Table 5A. Emission region parameters

source	xoffset	yoffset	R	n_{vol}	M	M_{Jeans}	M_{vir}	α_{vir}
	"	"	(pc)	(10^3 cm^{-3})	(M_{\odot})	(M_{\odot})	(M_{\odot})	
(1)	(2)	(3)	(4)	(5)	(6)	(7)	(8)	(9)
G004.15+35.77.1	150	-176	1.14	2.01	832	118	401	0.48
G004.17+36.67.1	36	1	1.24	0.79	419	22	104	0.25
G004.54+36.74.1	23	62	1.26	0.74	413	32	136	0.33
G004.81+37.02.1	236	-57	1.89	0.88	1661	82	405	0.24
G006.04+36.74.1	122	-245	0.63	2.68	188	39	116	0.62
G008.43+36.35.1	64	-68	0.33	2.07	21	7	18	0.89
G011.40+36.19.1	-88	39	0.45	1.62	41	25	53	1.27
G089.03-41.28.1	-81	-62	0.38	3.66	56	392	361	6.41
G101.62-28.84.1	72	318	0.63	0.70	49	43	80	1.65
G101.62-28.84.2	-21	81	0.73	0.62	67	33	76	1.13
G101.62-28.84.3	-23	-117	0.78	0.48	63	47	91	1.44
G102.72-25.98.1	125	-29	1.40	0.56	434	347	657	1.51
G145.08-39.30.1	-93	-30	0.43	3.16	70	38	83	1.18
G151.58-38.58.1	-53	214	0.20	2.32	5	17	20	3.79
G151.58-38.58.2	-58	-9	0.39	1.41	23	41	61	2.60
G151.58-38.58.3	233	-300	0.25	1.69	7	137	92	12.53
G151.58-38.58.4	-352	6	0.16	2.53	3	164	76	26.23
G153.74+35.91.1	-15	152	0.29	1.33	9	22	29	3.24
G156.42+32.53.1	232	-108	0.11	2.03	1	17	11	14.72
G158.77-33.30.1	-127	-111	0.54	4.10	181	222	367	2.03
G158.88-34.18.1	-95	122	0.76	1.84	226	32	108	0.47
G158.88-34.18.2	133	-90	1.00	1.60	447	132	352	0.79
G158.97-33.01.1	-129	1	0.17	1.69	2	17	15	6.55
G159.23-34.49a.1	87	44	1.46	2.08	1813	181	685	0.38
G159.23-34.49b.1	0	62	0.54	1.15	50	149	184	3.64
G159.41-34.36.1	-103	-146	1.02	1.80	533	55	205	0.38
G159.58-32.84.1	-16	95	0.25	0.91	4	111	64	16.05
G159.67-34.31.1	25	41	0.33	3.30	33	54	81	2.45
G160.64-35.04.1	-65	272	0.41	1.24	24	17	34	1.43
G160.64-35.04.2	-78	-116	0.66	0.68	54	48	89	1.63
G160.64-35.04.3	-288	31	0.50	0.80	28	43	67	2.39
G161.43-35.59.1	66	186	0.75	0.89	106	42	101	0.95
G161.43-35.59.2	36	-22	1.03	1.05	320	15	72	0.23
G161.85-35.75.1	-63	14	0.81	1.04	155	30	92	0.60

NOTE—All of the cores are shown in the table.

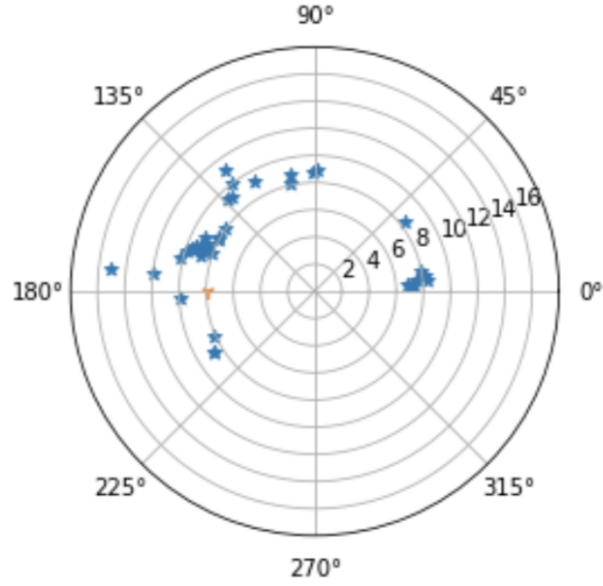


Figure 1. Face-on map of all 41 HGLCs. Blue ★ represent the clumps and yellow ★ is the location of our sun.

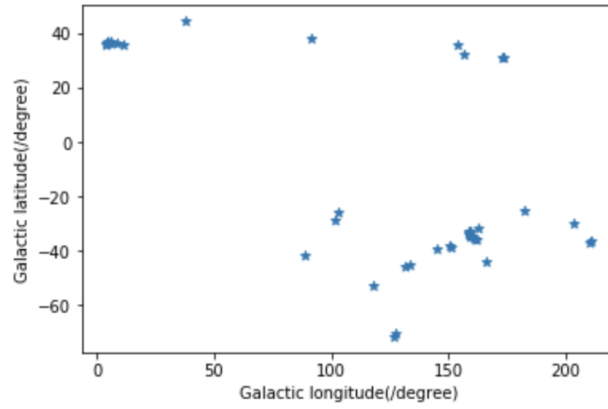


Figure 2. Long-Latitude coordinates map of all 41 HGLCs. Blue ★ represent the clumps. 41 clumps are seemingly centered into two groups: one at positive latitude ($b > 0$) and one at negative latitude ($b < 0$)

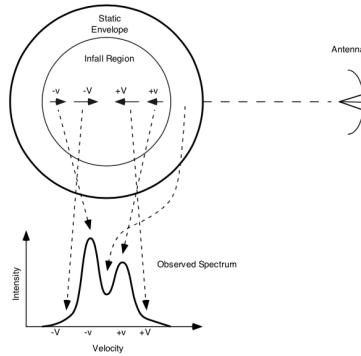


Figure 3. The origin of various parts of the line profile for a cloud undergoing inside-out collapse. The static envelope outside the infall region produces the central self-absorption dip, the blue peak comes from the back of the cloud, and the red peak from the front of the cloud. The faster collapse near the center produces line wings, but these are usually confused by outflow wings (Reference: Neal J. Evans II, 2002)

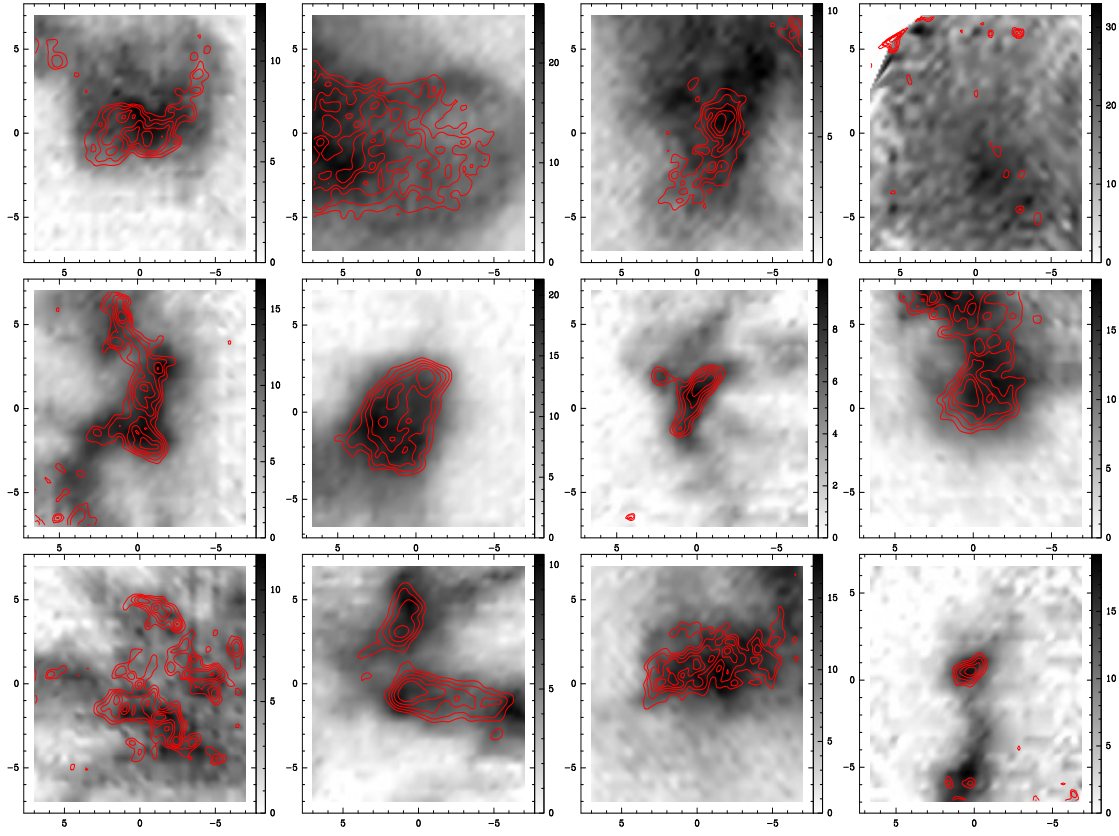


Figure 4. The examples of velocity-integrated intensity maps. The integrated intensities of ^{13}CO are represented as red contours stepped from 30% to 90% by 10% of the peak value. Gray scale is the integrated intensity of ^{12}CO .